INTERNATIONAL JOURNAL OF INTELLIGENT CONTROL AND SYSTEMS
VOL. 11, NO. 2, JUNE 2006, 97-105

Residual Vibration Analysis and Suppression for SCARA Robots in Semiconductor Manufacturing

WeiMin TAO, MingJun ZHANG, Ou MA and XiaoPing YUN

***Abstract*—This paper investigates residual vibrations of industrial SCARA robots in wafer handling applications. Due to rapid point-to-point movements, SCARA robot arms exhibit large vibrations after reaching the destination position. A mathematical model particularly suitable for residual vibration analysis is developed. The validity of the mathematical model is confirmed by the close match between experimental results and robot arm trajectories generated by the model. The root cause of residual vibrations is analyzed using the model. Based on the root cause analysis, a practical solution to suppress vibrations is proposed. The solution utilizes an acceleration smoother to smooth the commanded trajectory, and it can be easily implemented in practice without redesign the robot hardware or control system. Experimental results show over 40% reduction in both vibration amplitude and settling time.**

***Index terms*—Industrial robot, Vibration, Modeling, Control.**

1 INTRODUCTION

The robots studied in this paper refer to industrial SCARA (Selectively Compliant Articulated Robot Arm) robots for wafer handling as show in Fig. 1. Rapid point-to-point movements for the robot arms are usually involved in manufacturing environments. To transfer a wafer from one point to another, the robot arm needs to go through a series of motions involving accelerating to a required operational speed and decelerating to a full stop. The abrupt changes in acceleration or deceleration often result in residual vibrations. Figure 1 shows a laser recorded vibration plot (scale: 0.4mm/div) at robot's end-effector after the arm reachs the destination. The vibration may cause wafer slippery and lead to long system settling time.

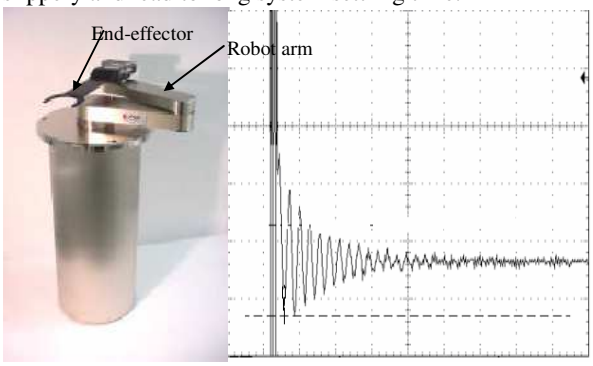

Fig. 1. A SCARA industrial robot and residual vibration.

To improve quality and efficiency of the manufacturing process, it is desired to understand the dynamics involved in the process and to develop efficient methods to suppress the vibration. The first thing is to identify the root cause of the vibration by creating and studying its dynamics model. Unfortunately, no well-developed models for studying the residual vibration of such robot arms are available in the open literature. The existing techniques of modeling SCARA robots are mainly for motion control as opposed to vibration control. In this paper, a dynamic model for vibration study of this type of industrial robots is first presented. Based on the dynamics model, a solution is then proposed to suppress the vibration. The dedicated modeling provides a good reference for similar industrial robots. The generic solution for vibration suppression can also be applied to other industrial applications.

The robot arm discussed here is driven by DC motors with high gear ratios for power transmission. The end-effector in the robot arm is connected to the motor through a number of pulleys. The pulleys are connected through timing belts. One advantage of this type of indirect drive system is its variation-isolation effect since the inertial changes on the payload have little effect on the actuator due to high reduction ratio. Besides backlash and additional friction in the transmission system, another disadvantage of the indirect drive system is that the lumped elasticity of the transmission system makes the robot arm work like a flexible manipulator and isolates the direct motor control and position feedback from the robot's end-effector. The residual vibration resulting from the elasticity (translation or rotation spring impact of the timing belt) of the transmission system sometimes becomes quite significant in a high-speed point-to-point motion. There are a couple of existing approaches to reduce or eliminate the vibration of a flexible structure:

- Increase damping by structural design or adding dampers: to ensure big damping, high natural frequency and stiffness [1][2];
- Open loop approaches: including trajectory smoothing input shaping and feed-forward approaches. The typical *trajectory smoothing* approaches (also called S-curve motion profiling) employ a multi order polynomial in time for trajectory generation [3][4]. Trajectory smoothing reduces the residual vibration by providing a smooth acceleration/deceleration and accounting for motor amplifier's electrical saturation feature. *Input shaping* approach convolves a sequence of impulses to produce a shaped input as the motion command. It reduces residual vibration by generating an input that cancels its own vibration [5][6][7][8]. *Feed-forward*

WeiMin Tao is with Brooks Automation Inc. USA (e-mail: dtao6@yahoo.com); MingJun Zhang is with Agilent Technologies, Plao Alto, USA (e-mail: zhangmingjun@ieee.org); Ou Ma is with New Mexico State University, USA (e-mail: oma@nmsu.edu); XiaoPing Yun is with Naval Postgraduate School, Monterey, USA (e-mail: yun@ieee.org).

approaches typically make use of input and model information to generate control output and to make the plant follow the predefined vibration free trajectory [9][1]. The open-loop approaches have to work with close-loop control to achieve other control objectives such as steady-state accuracy, system stability and robustness against disturbances and uncertainties.

- Close-loop approaches, such as conventional PID control, adaptive PID control, model based adaptive control [10][11][12][13], and H_∞ control design [14]. Due to the position difference of the end point (e.g. end-effector) and the controlled point (e.g. robot joint) of a flexible structure, the traditional collocated control often failed to achieve satisfactory performance. Non-collocated control approaches have been proven to have better control performance including vibration suppression [15][16][17]. However, this kind of approaches require additional sensors at the end point.

The trajectory smoothing approach is one of the most popular approaches currently used in industry. This is mainly due to its simplicity, flexibility and universality. PID feedback control is a primitive and robust robot control approach, which is easy to implement and can provide satisfactory control performance for varied dynamic characteristics. Other approaches may require accurate models, additional sensors, and/or intensive computations.

In this paper, the PID control and a generic motion profile (S-curve) are applied to the robots to meet the general requirements. The reason for selecting PID control approach is its robustness and simplicity. The reason for selecting the S-curve trajectory smoothing approach is, in addition to other benefits mentioned above, that the PID approach is incapable of keeping the system in critically damped condition, which is important to eliminate or reduce the vibration. This incapability is mainly due to implementation constraints (tracking error limit, electrical noise etc). The selected control scheme is able to meet most application's requirements. However, for some applications, which require very smooth motion with very high speed, the existing motion profile and control parameters fail to provide acceptable performance. The goal of this study is to resolve such an industrial problem by analyzing the root cause of the vibration problem and providing a practical and robust solution to the problem. For root-cause analysis, a dedicated dynamics model of the SCARA arm set is created. The root cause of arm vibration after motion completion is analyzed based on this model. The modeling of the arm set mainly takes into account factors of belt spring impact and damping friction. Lagrange formulation is applied for modeling the dynamics. A practical solution to reduce the residual vibration is proposed and evaluated.

The rest of the paper is organized as follows. Section 2 provides the modeling of the inherent dynamics of the robot arm with its parameters determined in section 3 using direct measurement and system identification. Section 4 conducts the root cause analysis of the vibration. Section 5 proposes a practical solution to suppress the residual vibration. The test results with two robots are presented in Section 6. Section 7 concludes the paper.

2 MODELING OF THE ROBOT ARM

2.1 SCARA Arm Robots

The modeling of the arm set in this work is mainly for vibration analysis instead of for motion control. Some assumptions in the modeling are made solely for the residual vibration analysis.

Figure 2 shows the kinematic notation of a general 3-DOF SCARA robot, where parameters L_i, l_i, m_i, I_i are defined respectively as link *i*, distance between mass center and the inboard joint of link *i*, mass of link *i*, and moment of inertia of link *i* (with respect to their respective rotational shafts parallel to Z axis). Link 1 (L_1) is the inner (or lower) arm; link 2 (L_2) is the outer (or upper) arm; and link T (L_t) is the end-effector.

The centerline of link i is the line connecting the two centers of the two half rounds (also the center of the pulleys) at the end of the link.

Θ_1 is the angle between the centerline of the inner arm and reference X-axis.

Θ_2 is the angle between the centerline of the outer arm and the centerline of inner arm.

Θ_T is the angle between the centerline of the end-effector and the reference X-axis.

ϕ is the angle between centerlines of outer arm and end-effector. For any static position under discussion, ϕ is a constant.

A cylindrical coordinate system is used to describe the robot's coordinates. For any point P we have:

- *R* is the distance from O (origin) to P', the orthogonal projection of the point P onto the XY plane. This is the same as the distance of P to the z-axis. The R axis is along the OP' line and points from O to P'.
- *T* is the angle between the positive X-axis and the line OP', measured anti-clockwise. T axis overlaps with z-axis.

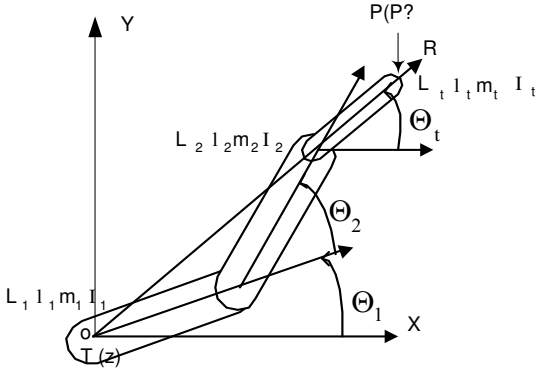

Fig. 2. The SCARA Arm Set.

- Z is the same as z.

The rotations of inner arm and outer arm are coupled by the belt-driving system such that the centerline of the end-effector axis always passes through the origin point O. So we define R axis as the radial axis from O to the centerline of the end-effector. The end-effector can only move along the R, T and Z axes. Θ_T is actually the rotational angle of end-effector around T axis, which is determined by the rotation of robot column bound with one end of the inner arm.

The residual vibration occurs after the arm reaches the destination position. In order to investigate the motion of the tip of end-effector after that, we make the following assumptions:

- The motion of the tip of end-effector to be investigated starts after the arm reaches the destination, which means the reference time of interest starts at the moment when the arm reaches the destination.
- The active torque from the motor and static friction approximately equal to zero after the arm reaches the destination.
- After the arm reaches the destination, the robot column and the inner arm that is connected to the column, completely stop moving.

Since the inner arm is not moving after the arm reaches the destination, the motion of the tip of end-effector is purely the combined motion of the outer arm and end-effector. The outer arm is connected through the belt B1 (located in inner arm) to the column; while the end-effector is connected through the belt B2 (located in outer arm) to the pulley, which is connected to the inner arm as shown in Fig. 3.

The T motor is connected to the robot column and R motor is connected to link 1. Both motors drive the T/R axes through a number of timing belts with a big gear ratio. T rotation drives both the robot column and link 1. R rotation causes rotations in link 1, link 2 and link T through B1 and B2 to ensure that the centerline of link T always passes through the origin O. Apparently the motors do not directly control the end-effector.

We assume that both the column and inner arm that is bound to the column have completely stopped after the arm reaches the destination. Then L_1 is motionless and the motions of L_2 and the tip of the end-effector are restricted by B1 and B2 due to their spring impact.

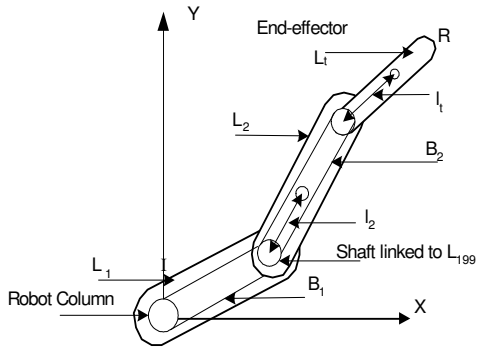

Fig. 3. Outer arm and end-effector connected by B1 and B2.

Two generalized coordinates are chosen to represent the vibration from robot's static pose:

- $q_1 = \theta_2$: The angle between the centerline of outer arm and its static position (corresponding to the given T/R destination position). This is the vibration angle resulting from the rotational stiffness of B1.
- $q_2 = \theta_t$: The angle between the centerline of the end-effector and its static position with respect to L2 (corresponding to the given T/R destination position), which maintains the same ϕ for any θ_2. This is the vibration angle resulting from the rotational stiffness of B2.

Figure 4 shows the geometric relationship between the arm's final static position (S) and dynamic vibration position (D). Both arms' positions are shown by the solid centerlines of L_1, L_2 and L_t. Assuming the arm's static position for the given T/R destination position is:

$$\begin{cases} \Theta_{1s} = \alpha_1 \\ \Theta_{2s} = \alpha_2 \\ \Theta_{ts} = \alpha_t \end{cases}$$

where $\alpha_1, \alpha_2, \alpha_t$ are constant angles. For any dynamic vibration position, we have:

$\theta_2 = \Theta_2 - \alpha_2$ and $\theta_t = \Theta_t - \alpha_t - \theta_2$

$\phi = \alpha_1 + \alpha_2 - \alpha_t$

The angular velocities are $\dot{\theta}_2$ and $\dot{\theta}_t$

2.2 *Lagrange's Equations*

It can be seen that B1 and B2 are not inter-connected; hence their motion due to belts' elongation is independent. However, since end-effector is mounted on L_2, the motion of the tip of end-effector results from the combined motion of both L_2 and L_t.

The kinetic energy of L_2 and L_t is as follows:

$$K = \frac{1}{2} m_2 V_{2c}^2 + \frac{1}{2} I_2 \dot{\theta}_2^2 + \frac{1}{2} m_t V_{tc}^2 + \frac{1}{2} I_t (\dot{\theta}_2 + \dot{\theta}_t)^2 \qquad (1)$$

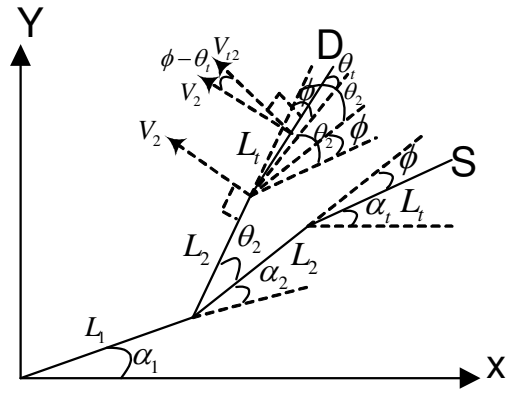

Fig. 4. Geometric relationship of the static and dynamic positions.

where I_2 and I_t are the moments of inertia with respect to the axes passing through the mass centers of L_2 and L_t, respectively. V_{2c} and V_{tc} are the respective velocities of the mass centers of L_2 and L_t.

Assume that the mass centers of L_2 and L_t are along their respective axis (symmetric mass distribution) and their distances to the center of rotation shaft are l_2 and l_t (shown in Fig. 3). The velocity of mass centers of L_2 and L_t can be computed based on the geometric relationship of L_2 and L_t shown in Fig. 4. V_{tc} is the sum of V_2 ($=\dot{\theta}_2 l_3$, the velocity at the rotation shaft of L_t) and V_{t2} ($=\dot{\theta}_t l_t$, the relative velocity of L_t with respect to L_2). We then have:

$$V_{2c} = l_2 \dot{\theta}_2 ;$$

$$V_{tc}{}^2 = (\dot{\theta}_2 l_3)^2 + (\dot{\theta}_t l_t)^2 - 2\dot{\theta}_2 l_3 \dot{\theta}_t l_t \cos(\phi - \theta_t)$$

where l_3 is the distance between the center of the rotation shaft of L_t and the center of rotation shaft of L_2. Generally, we have $\phi >> \theta_t$ (the vibration angle is relatively small in most discussed arm positions). Thus, $\cos(\phi - \theta_t) \approx \cos\phi$.

The potential energy of L_2 and L_t is mainly from the two belts B1/B2:

$$P = \frac{1}{2} k_1 \theta_2{}^2 + \frac{1}{2} k_2 \theta_t{}^2 \qquad (2)$$

where k_1 and k_2 are respectively the rotational stiffness of B1 and B2.

The Lagrangian becomes

$$L = K - P$$

The Rayleigh Dissipation (R) function is:

$$R = \frac{1}{2} c_1 \dot{\theta}_2{}^2 + \frac{1}{2} c_2 \dot{\theta}_t{}^2 \qquad (3)$$

where c_1 and c_2 are the lump sum damping coefficients of L_2 and L_t respectively.

The Lagrange's equation can be written as:

$$\frac{d}{dt}\left(\frac{\partial L}{\partial \dot{q}_i}\right) + \frac{\partial R}{\partial \dot{q}_i} - \frac{\partial L}{\partial q_i} = M_i \quad \text{for i=1 and 2.} \qquad (4)$$

where, M_i (for i=1, 2) are the torques applied to L_2 and L_t respectively. M_1 includes motor torque M_m and static friction torque. M_2 is only static friction torque. Applying (1)-(3) to the Lagrange's equation in (4), we have:

$$\begin{cases} (m_2 l_2{}^2 + I_2 + I_t + m_t l_3{}^2)\ddot{\theta}_2 + \\ (I_t - m_t l_3 l_t \cos\phi)\ddot{\theta}_t + c_1\dot{\theta}_2 + k_1\theta_2 = M_1 \\ (m_t l_t{}^2 + I_t)\ddot{\theta}_t + \\ (I_t - m_t l_3 l_t \cos\phi)\ddot{\theta}_2 + c_2\dot{\theta}_t + k_2\theta_t = M_2 \end{cases} \qquad (5)$$

It is noted that ϕ is constant for a given destination position. As a result, Eq. (5) represents a two-input two-output linear system.

3 PARAMETER DETERMINATION

3.1 Measurement and Experiment

Through measurements and experimental tests, we have obtained the following parameters show in table 1.

Table 1. Physical Parameters of A SCARA Robot

m_2	0.533 kg
m_t	0.533 kg
l_2	0.115 m
l_t	0.095 m
I_2	0.0035 (kg.m2)
I_t	0.00137 kg.m2
l_3	0.19 m

In (5), c_1, c_2 k_1, and k_2 are unknown parameters. Though translational spring constants of B1/B2 can be obtained through experiment, it's still a challenge to compute the rotational stiffness due to the difficulty in determining the tooth stiffness. In order to identify the above unknown parameters, we use system identification approach to compute them based on testing data.

3.2 System identification

MatLab System Identification programs are developed to calculate the four unknown parameters. First, we write the Eq. (5) in a state space form. We define the following state variables:

$$x_1 = \dot{\theta}_2; x_2 = \dot{\theta}_t; x_3 = \theta_2; x_4 = \theta_t$$

The state space equation is :

$$\begin{cases} \dot{X} = AX + BU \\ Y = CX + DU \end{cases} \qquad (6)$$

where, $X = [x_1\ x_2\ x_3\ x_4]^T$ and $Y = [\,x_3\ x_4\,]^T$

To investigate the motion after the arm reaches the destination, we assume that the active torque from motor and static friction are negligible (measurement of motor current verified this) and the end-effector motion is purely dominated by the initial condition of X, spring impact of B1/B2 (rotational stiffness), viscous friction, and the inertial of L_2 and L_t. In this case, U in Eq. (6) is zero.

The actual output data Y (θ_2 and θ_t) are computed from recorded laser data θ_2 and $\theta_2 + \theta_t$. The output data and the initial values of X are applied to Eq. (6) by the system identification program, and the unknown parameters of **A** in equation (6) are identified using PEM function in MATLAB (The function PEM provides an unbiased estimation method), and then the unknown parameters c_1, c_2, k_1 and k_2 are obtained. Below is a set of identified parameters for one of the robots:

c_1=0.293; c_2=0.1; k_1=439; k_2=167.5

After parameter estimation, the model outputs are

compared with the actual output data to verify the system identification results. Both back validation and cross validation are performed. Back validation compares the model output with the actual output driven by the data used for system identification. Figure 5 shows the back validation of end-effector vibration. The Y-axis is the output of $\theta_2 + \theta_t$ in radian; X-axis is the time in second. The black plot is real test data; the grey plot is the model output.

The back validation shows fairly good matching between the model output and the actual output.

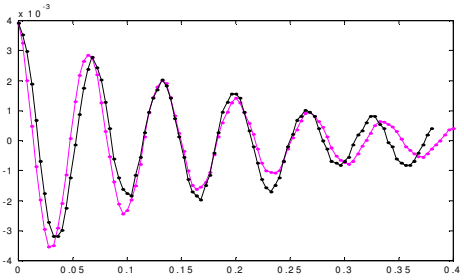

Fig. 5. Back validation of end-effector vibration.

The cross validation is also conducted for model verification. Cross validation compares the model output with the actual output driven by the data not used for system identification. The cross validation results also show a good match between model output and actual output except for the cases with small vibration amplitude. The main reason could be that with small vibration amplitude other factors which are not taken into account in the arm modeling become dominant, e.g., the small vibration resulting from the belts which connects T/R motors to robot column and L_1, static friction and non-linearity factors.

4 ROOT CAUSE ANALYSIS

4.1 *Output Analysis*

Intuitively we can see that the rotational spring impact of the timing belts plays a major rule in converting the potential energy to the kinetic energy and vice versa, which causes the residual vibration at the end-effector. This perception can be explored by investigating the transfer function of the output θ_2 and θ_t to the motor torque input M_m, which can be expressed as follows:

$$\theta_2(s)/M_m(s) = \frac{0.00289S^3 - 0.008892S^2 + 423.2S - 10580}{S^4 + 16.16S^3 + 157100S^2 + 1695000S + 1275000000}$$

$$\theta_t(s)/M_m(s) = \frac{0.00105S^3 - 0.05101S^2 + 163.4S - 3268}{S^4 + 16.16S^3 + 157100S^2 + 1695000S + 1275000000}$$

After the robot arm reaches the destination, the motor torque and the static friction torque are considered as zero. The outputs θ_2 and θ_t depend mainly on their initial condition and poles of their transfer function. The denominator polynomial of the transfer function is of the forth order. Its coefficients are functions of the spring rotational stiffness of B1 and B2, viscous damping coefficients and the inertial of L_2 and L_t. These coefficients determine the poles' location of the denominator polynomial. The vibration characteristics are also determined by those factors.

Analyzing the transfer function of $\theta_2(s)/M_m(s)$, it can be seen that there are two poles (far from the real axis) compensated by two zeros and two dominant poles very close to the imaginary axis. Figure 6 shows the pole and zero location of $\theta_2(s)/M_m(s)$. The pole location of $\theta_2(s)$ is the same as $\theta_t(s)$. The small squares are the poles and circles are zeros. Apparently the two dominant poles are very far from the critical damping ratio region (the sector bounded by the two bold lines), which indicates that the arm's damping ratio is extremely small and failed to quickly damp out the vibration caused by the rotational spring impact of B1/B2. The insufficient damping in the arm is the root cause of the vibration.

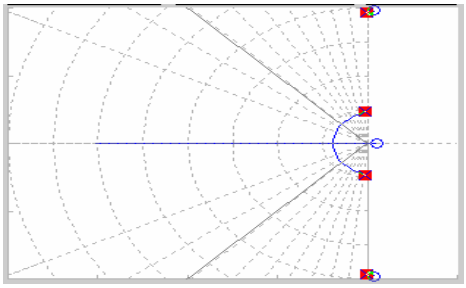

Fig. 6. The poles location of $\theta_t(s)$.

4.2 *Tooth engagement*

Detailed measurements of the arm vibration show that the vibration amplitude and settling time of the end-effector vary with respect to the arm positions in a fine scale. Figure 7 below shows the vibration amplitude data of four robots measured by laser position detection device.

The horizontal axis is the arm extension position in R direction. The vertical axis is the maximum vibration amplitude after the arm reaches the destination position. It can be seen that the vibration amplitude of all four robots varies with respect to the arm extension position in a similar cyclic pattern. The settling time also exhibits a similar pattern.

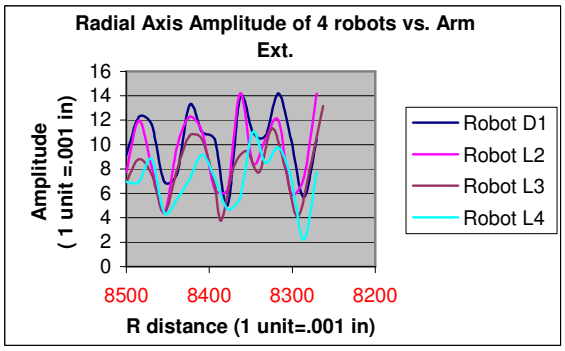

Fig. 7. The Vibration Amplitude Graph.

To analyze the power spectrum details of the vibration amplitude, a Fast Fourier Transform (FFT) is conducted with a typical result as shown in Fig. 8.

The power spectrum is expressed in terms of encoder counts per cycle. All four robots show the maximum power in 565 encoder counts, which means the dominant vibration cycle is 565 motor encoder counts. The number is very close to the teeth span of second pair of pulleys (and its related timing belt), which is 571 encoder counts. As such, a rational explanation is that the belt tooth engagement with pulleys create uneven torque to the motor, and the different engagement positions result in different initial vibration conditions (amplitude and its rate), which affect vibration after the arm reaches its final position.

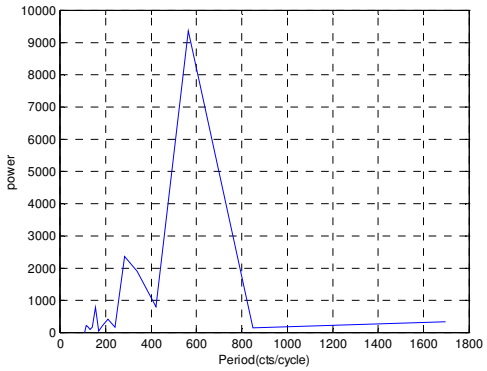

Fig. 8. FFT spectrum graph.

5 THE SOLUTION FOR SUPRESSING THE RESIDUAL VIBRATION

One major difficulty with our vibration suppression problem is that the end-effctor is indirectly controlled by the motors through a number of timing belts. As such, the current collocated control cannot directly increase the damping ratio of the arm set. The non-collocated approaches are not realistic at present due to the difficulty in adding additional sensors in the end-effector. Other model-based open or close loop approaches are also difficult to implement due to the model complexity, variable mass configuration (with or without wafer at the end-effector) and the constraint in redesigning the controller (involving substantial resource and qualification). To seek a practical solution, our focus is then put on providing a smooth input data, which will not excite vibrations unacceptable by applications.

In order to resolve the vibration problem, an acceleration smoother is proposed in this paper in addition to the conventional PID tuning. Figure 9 shows the diagram of the acceleration smoother and PID controller. This acceleration smoother is embedded in the commanded position (trajectory) generator, which does not involve a redesign of the controller. The testing results have shown good improvement and negligible side effects.

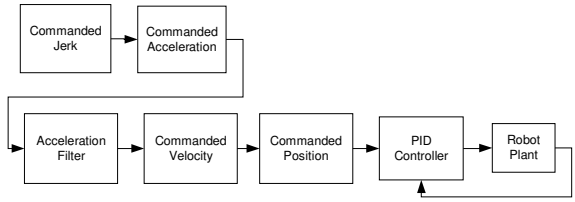

Fig. 9. The solution for vibration suppression.

Although tuning the PID controller cannot directly increase the damping of the co-located part of the robot arm, it can reduce the vibration by providing a smoother motor output. In other words, PID tuning can increase the system's damping ratio, which has an indirect impact on robot arm's vibration. By decreasing the proportional gain (K_p) and increasing the derivative gain (K_d) we are able to increase the damping ratio of the close loop motor system. However, tuning K_p and K_d subjects to other performance constraints. Reducing K_p results in big position-tracking error and increasing K_d causes electrical noise in the amplifier board. The final result for T/R axes is to reduce K_p from 45/60 to 35/30 and increase K_d from 180/240 to 300/400. The integral gains remain unchanged.

5.1 Acceleration smoother in Trajectory Generator

The PID tuning fails to achieve desirable vibration reduction performance since it cannot directly increase the damping ratio of the arm set and its tuning subjects to other constraints (e.g. electrical noise and position tracking error). To further improve the vibration suppression performance, an acceleration smoother is proposed to provide a smooth motion profile. By eliminating the abrupt change in the acceleration, a smoother commanded input can be generated, which in the end results in substantial vibration reduction at the end-effector.

The conventional S-curve motion profile most popular in industries is the third order trajectory generator with abrupt transitions in the acceleration as shown in Fig. 10.

In Fig.10, "j" is commanded jerk, "a" is commanded acceleration; "v" is commanded velocity and "x" is commanded position. In this case, changing the "j" value changes the acceleration ramp. However, adjusting j does not eliminate the sharp transitions in acceleration and hence is not able to significantly reduce the vibration unless j is substantially small resulting in substantially slow motion.

The idea of digital acceleration smoother is to smooth the sharp transitions in acceleration/deceleration to reduce the vibration without much loss in motion time. The acceleration plot in Fig.10 shows this, where the sharp transition corners are eliminated by the smooth transition curves as shown by the acceleration plots before/after smoothing.

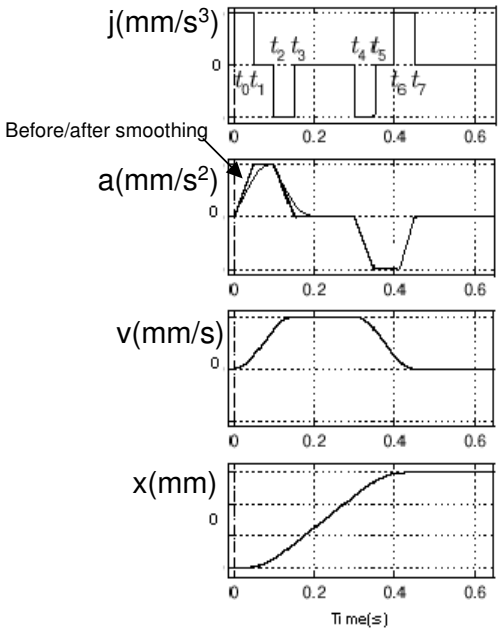

Fig. 10. Third Order Trajectory Generator.

The digital acceleration smoother is actually a first order filter modeled as:

$$\frac{U_0(Z)}{U_i(Z)} = \frac{z}{z - e^{-\frac{T}{\tau}}}$$

where U_o is the commanded acceleration output; U_i is the commanded acceleration input; T is the sampling time interval; and τ is the time constant.

The time constant τ is to be designed to provide the desired performance. Selecting τ is a trade off between smoothness and speed. Currently it is set to 0.05 seconds to achieve significant vibration reduction without much impact on throughput.

5.2 Distinguished features of the acceleration smoother

The acceleration smoother can effectively reduce the vibration by smoothing out the acceleration/deceleration (hence to provide a smoother motion profile). There are two major differences between the proposed acceleration smoother and the conventional first order low pass filter. First, the acceleration smoother is not used for filtering the sensor output or reducing the control output jitter but is used for smoothing the commanded acceleration of the trajectory generator. Second, the acceleration smoother is not located after the sensor module or in the control loop but is located in the trajectory generator. So its implementation does not require the controller redesign.

There are two major advantages comparing to the multi-order S-curve motion profile (e.g. the 4th order trajectory generator in [3]). First, the acceleration smoother leads to a velocity profile with infinite order of smoothness (i.e. no abrupt transition in any order of its derivative); second, it's much easier to implement.

6 TEST RESULTS

6.1 Improvement in vibration amplitude and settling time

Two robots are tested with separated PID tuning, the acceleration smoother and the combination of them. Tests are conducted in 16 arm extension positions with equal position displacement set at 0.015 inches. The vibration amplitude is the maximum peak-to-peak amplitude of end-effector vibration, starting from motion completion time. The settling time is the time taken from motion completion time to the time when all the end-effector vibrations fall within a fixed threshold (set to 0.12mm in our tests). Figure 11 shows a sample comparison of End-effector vibration (recorded by laser detector) without and with acceleration smoother.

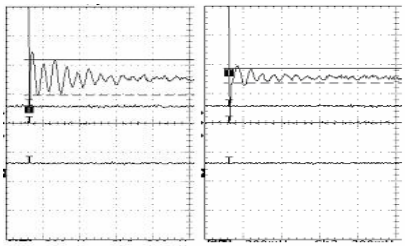

(a) (b)

(a) without acceleration smoother(b) with acceleration smoother

Fig. 11. Vibration Comparison.

Significant improvements are observed in both robots. PID tuning results in approximately 15% improvement in amplitude and 14% improvement in settling time. The acceleration smoother results in about 45% improvement in amplitude and 44% improvement in settling time. Improvements from PID tuning combined with the acceleration smoother results in approximately 55% improvement in amplitude and 54% improvement in settling time. Table 2 shows the detailed test results in comparison with the original controller (original PID parameter, no smoother).

Table 2. Improvement on Vibration Amplitude and Settling time

	Average amplitude for 16 arm positions (mm)		**Average settling time for 16 arm positions (ms)**	
	Robot1	Robot2	Robot1	Robot2
Original	0.280	0.570	164	611
Smoother	0.153	0.319	80	386
Average Improvement (%)	**45.3**	**44.1**	**51.2**	**36.7**
PID Tuning	0.252	0.450	157	469
Average Improvement (%)	**9.8**	**21.1**	**4.3**	**23.3**
Smoother + PID	0.133	0.230	74	279
Average Improvement (%)	**52.5**	**59.0**	**54.8**	**54.4**

6.2 Impact on throughput and repeatability

Smoothening acceleration/deceleration may cause longer commanded motion time. For a typical wafer handling motion and the given time constant of the acceleration smoother, there is a 3.45 % increment in the commanded motion completion time (30ms per motion), which will theoretically lead to a throughput loss of about 0.19% in a typical application (or 7.1 seconds per hour, assuming the tool throughput is 120 wafers/hour). However, the actual motion completion time is less due to shorter settling time resulting from the quickly decayed vibration. Further more, any throughput loss can be avoided by increasing the maximum commanded acceleration and speed value, which are no longer limited by the original vibration performance.

Testing with a laser repeatability fixture on two robots shows that 27% to 55% improvement in range and 3-sigma value is achieved.

7 CONCLUSIONS

This paper has presented a dedicated dynamic model for the SCARA arm set of an industrial robot. The goal of this modeling is to investigate the root cause of the vibration of the end-effector after the robot arm reaches the destination. The model parameters are obtained through system identification. Based on this model, root locus approach is used for analyzing vibration root cause. The model matches fairly well with the actual system. It has been concluded that

- The insufficient rotational stiffness of belts B1/B2 and insufficient damping ratio of the arm set are dominant factors for the vibration.
- The belt tooth engagement with the pulley causes the unevenness of the vibration with respect to the arm positions.

The root cause analysis shows that the residual vibration cannot be easily eliminated without drastic redesign of the robot system (e.g. using direct-drive control or adding additional sensors to the tip of the end-effector). Therefore, a practical solution called acceleration smoother is proposed and investigated. The test results showed that the residual vibration is significantly suppressed and robot motion repeatability is significantly increased without much impact on throughput.

The root cause analysis and vibration suppression solution proposed in this paper can effectively resolve an industrial problem. Consistent performance and reliability improvements have been achieved in practical applications. The new technique can make a good impact on the quality of wafer handling process in semiconductor manufacturing and bio-chip fabrication.

REFERENCES

[1] N Kim and M Hong, "Diagnosis and Reduction of Robot Arm Vibration for 12-Inch Wafer Spin Scrubber," *Trans Tech Publication 2004, Key Engineering Materials* Vols. 270-273, pp.884-889.

[2] J. Roy and L.L.Whitcomb, "Comparative Structrual Analysis of 2-DOF Semi-Direct-Drive Linkages for Robot Arms," *IEEE/ASME Transactions on Mechatronics*, Vol.4, No. 1, pp 82-86, 1999.

[3] P. Lambrechts, M. Boerlage and M. Steinbuch, "Trajectory Planning and Feedforward Design for High Performance Motion Systems," *Proc. of American Control Conference*, pp 4637-4642, 2004.

[4] P.H.Meckl and W.P.Seering, "Minimizing Residual Vibration for Point-to-Point Motion," *Journal of Vibration and Acoustics*, Vol.107, Oct. 1985, pp. 378-382.

[5] Singhose, W., Seering, W. and Singer, N., "Residual Vibration Reduction Using Vector Diagrams to Generate Shaped Inputs," *ASME Journal of Mechanical Design*, Vol. 116, pp. 654-659, June 1994.

[6] Singer, N.C. and W.P.Seering, "Preshaping Command Inputs to Reduce System Vibration," *ASME journal of Dynamic Systems, Measurement, and Control*, 112:pp.76-82, 1990.

[7]. Singhose, W. and Singer, N., "Effects of input shaping on two-dimensional trajectory following," *IEEE Transactions on Robotics and Automation*, Vol. 12, pp. 881-887, 1996.

[8] B.R. Murphy and J. Watanabe, "Digital Shaping Filters for Reducing Machine Vibration," *IEEE Transaction on Robotics and Automation*, Vol. 8, No. 2, pp.285-289, 1992.

[9]. A. Piazzi and A. Visioli, "Minimum-time system inversion based motion planning for residual vibration reduction," *IEEE/ASME Transactions on Mechatronics*, Vol. 5, pp. 12-22, 2000.

[10] McEver, M.A. and Leo, D.J., "Autonomous vibration suppression using on-line pole-zero identification," *ASME Journal of Vibration and Acoustics*, vol. 123, no. 4, pp. 487-495, 2001.

[11] Coyle-Byrne, J. and Klafter, R.D. "Real-time zone-adaptive control of SCARA-type robot arm," *Proceeding of ICRA 1990*, pp 2089-2094 vol.3, May 1990.

[12] Louis L. Whitcomb, Alfred A. Rizzi, and Daniel E. Koditschek. "Comparative experiments with a new adaptive controller for robot arms," *IEEE Transactions on Robotics and Automation*, Vol. 9, pp59-70, 1993.

[13] W. J. Book, O. Maizza-Neto, and D. E. Whitney. "Feedback Control of Two Beam, Two Joint Systems with Distributed Flexibility", *Journal of Dynamic Systems, Measurement, and Control* 97(4), pp424-431, 1976.

[14]. J. C. Doyle, K. Glover, P.P.Khargonekar, and B.A.Francis, "State-space Solutions to Standard H_2 and H_∞ Control Problems," *IEEE Transaction on Automatic Control*, Vol. 34, No. 8, pp. 831-847, 1989.

[15] Siciliano, B. and W. Book, "A Singular Perturbation Approach to Control of Lightweight Flexible Manipulators," *International Journal of Robotics Research*, vol. 7, no. 4, pp. 79-90, August, 1988.

[16] J.H.Ryu, D.S. Kwon and B. Hannaford, "Control of a Flexible Manipulator with Noncollocated Feedback: Time-Domain Passivity Approach," *IEEE Transaction on Robotics*, Vol. 20, No. 4, pp.776-780, 2004.

[17] V.A.Spector and H. Flashner, "Modelling and Design Implications of Noncollocated Control in Flexible Systems," *ASME Journal Dynamic Systems, Measurement, and Control*, Vol. 112, pp 186-193, 1990.

WeiMin Tao received the B.E degree in automation, M.E. and Ph.D. degrees in computer control and simulation from Beijing University of Aeronautics and Astronautics, Beijing, China, in 1982, 1988 and 1992, respectively.

From 1992 to 1997, he worked on optical-electronics control system in Singapore Technologies Inc.

From 1997 to 1999, he worked on multi-robot system R&D with DSO National Laboratories, Singapore.

Since 2000, he has been working on control and software development for industrial robotics with Brooks Automation Inc., USA.

MingJun Zhang received the D.Sc. degree from Washington University in St. Louis, USA. He was awarded the Early Career Award (industry) by the IEEE Robotics and Automation Society in 2003. He currently serves as an Associate Editor for the IEEE Transactions on Automation Science and Engineering, and is on the editorial board of Nanomedicine: Nanotechnology, Biology and Medicine. His current research interests include micro/nano-scale system dynamics and control, life science automation, and bio-instrumentation.

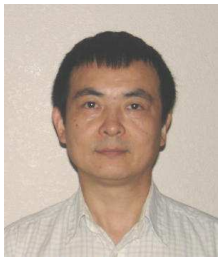

Ou Ma received the B.Sc. degree from Zhejiang University, China, in 1982 and M.Eng and Ph.D degrees in Mechanical Engineering from McGill University, Canada, in 1987 and 1991, respectively.

He is currently an associate professor in the Department of Mechanical Engineering, New Mexico State University. His research interests are in dynamics, control, and experimental verification of complex robotic systems. Prior to joining the Nex Mexico State University in 2002, Dr. Ma had been employed by MDA Space Missions (MD Robotics) of Canada for over ten years, working as a project engineer and R&D technical lead for developing modeling, simulation, and verification techniques for the space robots: Canadarm, Canadarm2 (SSRMS) and Dextre (SPDM). He is still actively conducting collaborative research with industry and government laboratories. Dr. Ma is a member of IEEE, AIAA, and ASME

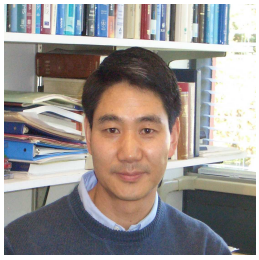

Xiaoping Yun is a Professor of Electrical and Computer Engineering at the Naval Postgraduate School at Monterey, California, USA. His research interests include coordinated control of multiple robotic manipulators, mobile manipulators, mobile robots, control of nonholonomic systems, MEMS sensors, carbon nanotubes-based sensors, and human body motion tracking using inertial/magnetic sensors. He holds B.S degree from Northeastern University, China, and M.S. and PhD degrees from Washington University in St. Louis, USA. He is a Fellow of IEEE.